


 Cite this: *RSC Adv.*, 2022, 12, 35383

# An effective antimicrobial complex of nanoscale $\beta$ -cyclodextrin and ciprofloxacin conjugated to a cell adhesive dipeptide†

 Reza Taheri-Ledari,<sup>a</sup> Farinaz Jalali,<sup>a</sup> Leili Heidari,<sup>ab</sup> Fatemeh Ganjali,<sup>a</sup> Fereshteh Rasouli Asl,<sup>a</sup> Simindokht Zarei-Shokat,<sup>a</sup> Mohadeseh Forouzandeh-Malati,<sup>a</sup> Adibeh Mohammadi<sup>a</sup> and Ali Maleki<sup>ib\*</sup>

Today, various drug delivery systems (DDS) are utilized to carry and deliver the desired drugs to the targeted action area to reduce potential side effects and negative interactions. Nanomaterials are an excellent candidate for the delivery of potent drugs, as they enhance pharmacokinetic and pharmacodynamic properties. Herein, we present a new ciprofloxacin (CPF) delivery system based on a polymeric nanocarrier ( $\beta$ -cyclodextrin) conjugated to a cell-adhesive dipeptide structure. Cyclodextrin (CD) is an inexpensive, easily accessible, biodegradable, and biocompatible material. Also, the conjugation of cysteine–arginine (CR) dipeptide to the CPF/ $\beta$ -CD particles is carried out to enhance cell adhesion growth. Through accurate analysis, the drug content and release for a final product have been estimated to be ca. 32%. Overall, the antimicrobial effects of CPF were considerably raised through a low dose of CPF. The growth zone inhibition of CPF/ $\beta$ -CD–CR particles on the *Staphylococcus aureus* and the *Escherichia coli* bacterial cells was  $5.5 \pm 0.2$  cm and  $3.5 \pm 0.2$  cm, respectively. Hence, this therapeutic nano bioconjugate is an excellent candidate to be applied in antimicrobial applications with the minimum incorporated CPF.

 Received 15th September 2022  
 Accepted 23rd November 2022

DOI: 10.1039/d2ra05822g

[rsc.li/rsc-advances](http://rsc.li/rsc-advances)

## 1. Introduction

Antibiotics are regarded as the most significant developments in the modern era of medicine because of their tremendous effect on the reduction of mortality in humankind as well as economic harm. Nowadays, antimicrobial resistance (AMR) is the most critical concern in the fight against infectious diseases caused by drug abuse.<sup>1–3</sup> Indeed, the mechanism of antibiotics action illustrates that antibiotics prevent the synthesis of the bacteria cell walls, disturb the cellular membrane, forbid the synthesis of nucleic acid,<sup>4</sup> inhibit protein synthesis, block pathways and disrupt metabolism.<sup>5</sup> Novel quinolones as antibiotics have been extended with enhanced effectiveness and spectrum over the years.<sup>6</sup> CPF is a second-generation fluoroquinolone used to treat various infections, including urinary infections, infections related to bone, cystic fibrosis, chronic otitis media, prostatitis, and so on.<sup>7,8</sup> CPF demonstrates more

remarkable activity against Gram-negative bacteria (Enterobacteriaceae like *Escherichia coli*) than Gram-positive bacteria (*Staphylococcus aureus*).<sup>9</sup> To clarify the antibacterial mechanism of the CPF, it is crucial to know that CPF is a DNA gyrase inhibitor. DNA gyrase is a tetramer consisting of two subunits GyrA and two GyrB subunits. DNA gyrase belongs to a group of enzymes called DNA topoisomerases, which is an essential part of the DNA replication system, and its function is to break the backbone of DNA. The GyrA subunit binds to DNA and hydrolyzes the backbone, while GyrB catalyzes the hydrolysis of ATP, which drives the supercoiling process. Topoisomerase IV is involved in resolving daughter chromosomes after DNA replication as well as the unscrewing of supercoils in the DNA. CPF do not play a role in the breaking reaction of DNA strands catalyzed by these enzymes but inhibit the recombination step. CPF are commonly bacteriostatic. However, high doses of CPF can lead to double-stranded DNA breaks that are lethal to the affected cells.<sup>10</sup>

In fact, one of the best ways to reduce interactions referred to drugs, diminish side effects, and increase the ability to kill bacteria is using appropriate DDS.<sup>11</sup> Drug delivery means the delivery of pharmaceuticals to a target tissue to achieve safer and better therapeutic outcomes.<sup>12</sup> DDS has some advantages and disadvantages, such as extending the duration of the action, reducing the frequency of dosage and ensuring the bioavailability of medicines, keeping the drug against

<sup>a</sup>Catalysts and Organic Synthesis Research Laboratory, Department of Chemistry, Iran University of Science and Technology, Tehran 16846-13114, Iran. E-mail: maleki@iust.ac.ir

<sup>b</sup>Department of Chemistry, Faculty of Basic Sciences, Ilam University, P. O. Box 69315-516, Ilam, Iran

† Electronic supplementary information (ESI) available: H-NMR spectra of the synthesized CR dipeptide structure and successively modified beta cyclodextrin. See DOI: <https://doi.org/10.1039/d2ra05822g>



degradation, minimize adverse drug side effects, enhance the compliance of patients and increase medication use through declining fluctuation plasma concentration. However, the disadvantages include the toxicity of the drug delivery device, the potential for hazardous degradation products, the need for surgery either on applying systems or removal, patients might be uncomfortable using the DDS device, and the cost and usage of DDS may be expensive.<sup>11</sup>

Nanotechnology affects everything from nanoscale gadgets to drug delivery frameworks.<sup>13–15</sup> Drug delivery to the pain site can be active or passive *via* nanocarriers. In active targeting, peptides and antibodies are conjugated to the DDS *via* targeted tissue receptors, lipids, or antigens. The conduction of drugs *via* the self-assembled nanostructured and released drug encapsulation at the object is related to passive targeting.<sup>16–18</sup> In the last few decades, the application of nanomaterials in a variety of scientific domains, including; catalysis,<sup>19–27</sup> photocatalysis,<sup>28,29</sup> gas adsorption,<sup>30</sup> applications in environments,<sup>31</sup> devices in photovoltaic and photoelectric,<sup>32,33</sup> and drug delivery has grown. There are different types of nanocarriers like; polymeric nanoparticles (NPs), magnetic nanoparticles (MNPs), gold nanoparticles (AuNPs), and mesoporous silica nanoparticles (MSNPs).<sup>34</sup> Preparing nanocarriers is crucial since many novel drugs have low solubility in water and low bioavailability.<sup>35</sup> Drug delivery has had a lot of development over the last few decades. As proven, biodegradable and bioabsorbable polymers provide a magical option for many novel DDS. For instance, CD derivatives are one of the natural polymers for polymeric drug delivery carriers.<sup>36</sup> CD-based nanocarriers can enhance the bioavailability, correct the metabolism of medication, toxicity decline, also boost the drug's half-life.<sup>37</sup>  $\beta$ -CD has a versatile potential with its suitable geometry for forming inclusion complexes with innumerable drugs.<sup>38</sup> Furthermore,  $\beta$ -CD is a good option for drug delivery because the size of the cavity (inner cavity diameter: 6.0–6.4 Å, outer diameter: 15.4 Å) is affordable, and the drug loading mechanism improves the bioavailability solubility and stability of cargo.<sup>39</sup> However, to enhance the accomplishment of these DDSs, nanocarriers may be fitted with attached proteins or chains of synthetic peptides.<sup>38</sup> Among various species of proteins, peptides do not damage the integrity of the cellular membrane.<sup>40</sup> The attendance of the specific amino acids in the formation of peptides, such as arginine, is crucial because of its cationic guanidine groups, which are able to interact with anionic sulfate or phosphate groups over the cell membrane.<sup>41</sup>

The study represents an efficient DDS construct from  $\beta$ -CD nano carriers covered by 3-mercaptopropyl trimethoxy silane (MPTMS) cross-linker to deliver the antibiotic CPFEX. Additionally, a new dipeptide structure, which has been synthesized in a solid phase, has been employed as an influential factor for penetrating the bacterial cells and better conjugating the structure. Notably, incorporating the peptides into the structure led to the CPFEX dosage reduction, even in connection with Gram-negative bacteria. Briefly, the zone of inhibition (ZOI), minimum inhibitory concentration/minimum bactericidal concentration (MIC/MBC), and colony count experiments were accomplished to evaluate the *in vitro* cellular experiments of

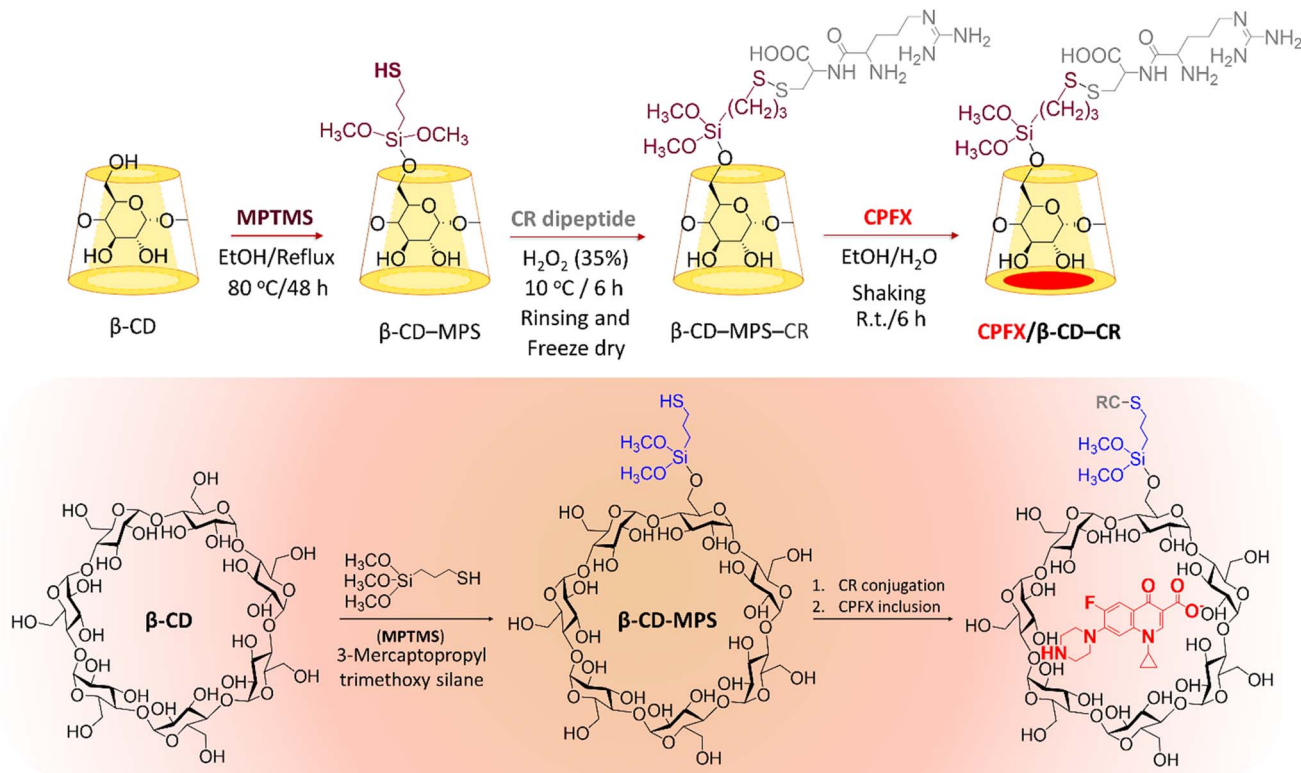
CPFEX/ $\beta$ -CD-CR on Gram-negative (*E. coli*) and Gram-positive (*S. aureus*) bacteria. Nanocarrier integration with the drug content of 32% has enhanced the antibacterial activity of the prepared nanocarrier in comparison with the individual analogous dosage of CPFEX. Notably, the derivatives of CD can use as anti-infective agents. Many CDs and their derivatives have low toxicity and resistance to enzymatic breakdown in biological fluids with GRAS (generally regarded as safe) status from the FDA. Moreover, we introduced the bacterial cellular uptake of CPFEX by conjugating a dipeptide to CPFEX/ $\beta$ -CD and its controlled release in different conditions.

## 2. Results and discussion

### 2.1. Preparation of CPFEX/ $\beta$ -CD-CR nanocomplex

In the first stage, the surface of  $\beta$ -CD was modified with MPTMS to introduce –SH groups onto the surface. In the third stage, the synthesized CR dipeptide is connected to the surfaces *via* the foundation of a disulfide bond (Scheme 1). The dipeptide is created from 2-chlorotriethyl chloride (CTC) resin through solid-phase synthesis.<sup>44</sup> In this regard, the resin was washed with dimethyl formamide (DMF) and dichloromethane (DCM) to provide a pure and inflated CTC complex. Following this, cysteine amino acid and *N,N*-diisopropylethylamine (DIEA) were mixed in the DMF, and all contents were shaken at room temperature (25 °C). Then, the capping step was completed *via* methanol solution; subsequently, the protection group of Fmoc was eliminated with a piperidine solution in the DMF (25%). Then a blend of arginine amino acid, DIEA, and *N,N,N',N'*-tetramethyl-*O*-(benzotriazole-1-yl)-uronium tetrafluoroborate (HBTU) has been appended to the system and shaken. Finally, the last deprotection was performed, and the CTC was separated *via* trifluoroacetic acid (TFA) (95%) from the complex. The structure of the synthesized CR dipeptide was confirmed by H-NMR spectroscopy (Fig. S1, in the ESI section†). To conjugate the CR dipeptide with the surface of the CPFEX, a disulfide bond has been constructed between the mercaptopropyl silane (MPS) and the cysteine amino acid thiol end groups. In this step,  $\beta$ -CD-MPS particulates have been dispersed into distilled water through an ultrasonic ice bath. Next, dropwise ethanol was added to a mixture of CR dipeptide solution with partial quantities of hydrogen peroxide. The CPFEX drug was loaded into the functionalized nanocarrier in the next stage. The inner cavity of  $\beta$ -CD is lipophilic, while the outer one is hydrophilic, which makes their complex formulation possible with lipophilic molecules. The  $\beta$ -CD can encapsulate molecules inside their cavity *via* non-covalent interactions such as electrostatic, van der Waals, hydrophobic, and hydrogen bonds to form an inclusion complex of host-guest type.<sup>42,43</sup> Moreover, computational modeling has shown that van der Waals forces are the most important driving forces for the complexation and the moiety (piperazinyl) of the CPFEX drug structure, which is included in the internal cavity of  $\beta$ -CD.<sup>45</sup> Consequently, through centrifugation, the CPFEX/ $\beta$ -CD-CR particulates were collected.<sup>46</sup> In order to verify the prepared structures within the preparation route (presented in Scheme 1), H-NMR spectra of the neat  $\beta$ -CD,  $\beta$ -CD-MPS, and CPFEX-included  $\beta$ -CD-MPS were prepared, as





Scheme 1 Schematic preparation of CPFX/β-CD-CR nanocomplex. Note: the “MPS” has been eliminated from final formulation (CPFX/β-CD-MPS-CR), as it does not play any significant role in the application.

well. However, for evaluation of the CPFX inclusion (and also CR conjugation) into the structure, the H-NMR spectrum of CPFX/β-CD-CR was provided, but it was crowded and not quite interpretable. In fact, the signals in the same chemical shift areas extensively overlapped in the H-NMR spectrum. Therefore, the H-NMR spectrum of “CPFX/βCD-MPS” complex as a clue on the preparation of CPFX/βCD-CR complex was provided, as it is less crowded and the signals related to the included CPFX are quite interpretable. However, the H-NMR spectrum of CPFX/β-CD-CR has also confirmed the presence of CPFX into the structure, where the signals related to the aromatic protons of CPFX have appeared between 6.0 and 8.0 ppm. Also, the observed integrated amounts of the protons in the mentioned area can be another verification for the CPFX inclusion. As exhibited in Fig. S2–S8 (in the ESI section†), all of the shown structures in the scheme are corroborated by the NMR data.

## 2.2. Characterization of CPFX/β-CD-CR nanocomplex

**2.2.1. Fourier-transform infrared spectroscopy.** The Fourier-transform infrared (FTIR) spectroscopy is a method used to acquire the infrared spectrum of absorption, emission, and photoconductivity of solid, liquid, and gas. It is utilized to distinguish various functional groups in the materials. As demonstrated in Fig. 1a, the broad pick at  $3400\text{ cm}^{-1}$  is related to the O–H bonds, and the peak of the C–H bond with hybridization  $sp^3$  appeared at  $2900\text{ cm}^{-1}$ , stretching vibrations. As well

as this, the peak of the bending vibrations of the C–H bond with hybridization  $sp^3$  emerged at  $1400\text{ cm}^{-1}$ , and peaks at  $1100\text{ cm}^{-1}$  showed C–O stretching.<sup>47</sup> In Fig. 1b, a sharp peak at  $1100\text{ cm}^{-1}$  and a peak at  $800\text{ cm}^{-1}$  are allocated to Si–O–Si and Si–O stretching vibrations, respectively. There is also a weak peak to illustrate the position of the mercapto (–SH) group at the absorption peak of  $2500\text{ cm}^{-1}$ .<sup>48</sup> Additionally, in Fig. 1c, another broad peak in the region of  $3400\text{ cm}^{-1}$  is represented by the N–H stretching group. In Fig. 1d, the band at  $1650\text{ cm}^{-1}$  exhibited C=O (carbonyl) and C=N stretching.<sup>49</sup> Among the vibrations, those at  $1100\text{ cm}^{-1}$  and  $700\text{ cm}^{-1}$  are assigned to the vibration absorption of C–N stretching and secondary amine, respectively.<sup>50</sup>

**2.2.2. Energy-dispersive X-ray spectroscopy.** Energy-dispersive X-ray spectroscopy (EDX) is based on the production of characteristic X-rays, highlighting the identity of the elements within the sample (Fig. 2). The attendance of O and C atoms has been verified in each of the specimens *via* the emerged signals at 0.5 and 1.8 keV, respectively. The existence of MPS was checked through a signal revealed at 2.3 and 1.7 keV (spectrum b), which is related to S and Si atoms, respectively. The only released electrons from the F atom (3.84% of the total weight) are referred to as CPFX (spectrum c). The peak intensity associated with carbon and sulfur components is gained by conjugating the CR dipeptide (spectrum d).

**2.2.3. Thermogravimetric analysis.** The thermal degradation state of the prepared CPFX/β-CD-CR nano-cargo was investigated by thermogravimetric analysis (TGA). Since the



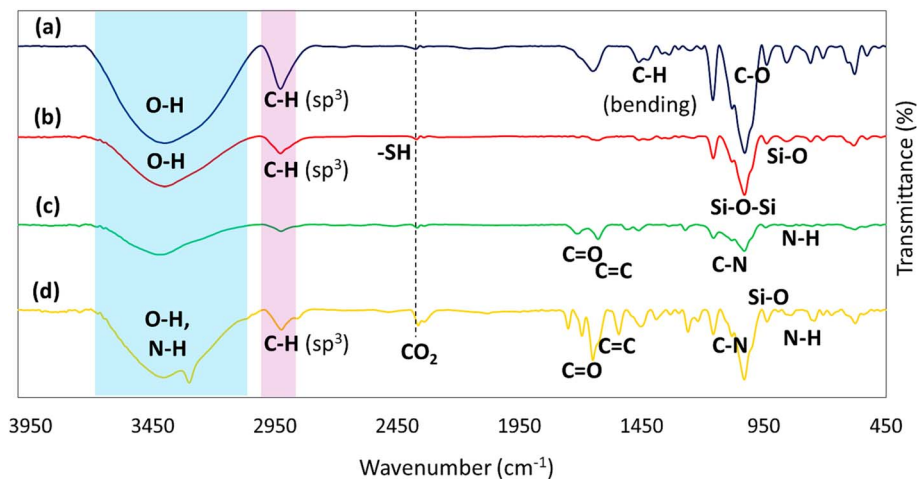


Fig. 1 FTIR spectra of (a)  $\beta$ -CD, (b)  $\beta$ -CD-MPS, (c)  $\beta$ -CD-MPS-CR, (d) CPFX/ $\beta$ -CD-CR nanocomplex.

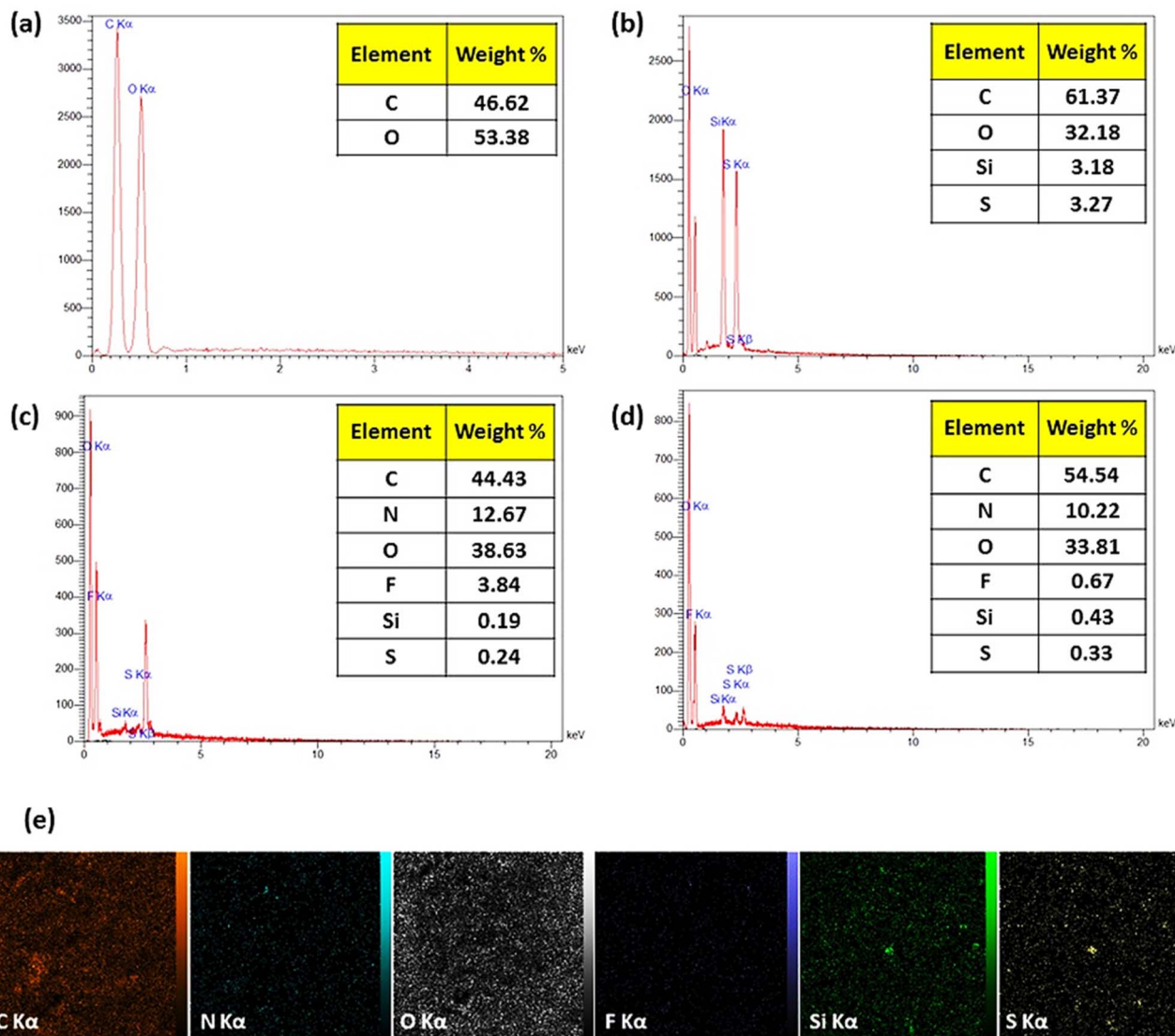


Fig. 2 EDX spectra and quantitative results of (a)  $\beta$ -CD, (b)  $\beta$ -CD-MPS, (c)  $\beta$ -CD-MPS-CR, (d) CPFX/ $\beta$ -CD-CR, (e) EDX mapping of the CPFX/ $\beta$ -CD-CR nanocomplex.



whole structure is made of a hydrocarbon skeleton, it was expected to see a rapid and complete degradation trend over the heating process.<sup>51</sup> As presented in Fig. 3a, the thermal degradation is initiated from 75 °C with a rel. mass value of *ca.* 113%, and continued to 600 °C. At first glance, this is assumed that an error has occurred in the data due to the excess 13 wt% at the beginning, but it is a typical occurrence in the polymeric hydrogel structures that a large volume of the moisture in the air is adsorbed by a partial increase in the temperature.<sup>52</sup> In the whole trend of degradation, this is observed that a 17% weight loss (113–96%) has occurred *via* heating the sample up to *ca.* 260 °C, due to the quick elimination of water molecules from surfaces and the underlying layers of CPFX/ $\beta$ -CD–CR nanocargo.<sup>53</sup> At the following stage, *ca.* 32% of the total weight (96–64%) disappeared in a thermal range of 260–290 °C. This fast drop in weight can be ascribed to the removal and degradation of the CPFX drug encapsulated into the polymeric  $\beta$ -CD strands.<sup>54</sup> Afterward, degradation of the  $\beta$ -CD–CR structure started from 300 °C and continued to *ca.* 600 °C, where the whole structure was mainly decomposed to CO<sub>2</sub> molecules. These results can essentially confirm the structural attributes of the CPFX/ $\beta$ -CD–CR nanocomplex.

**2.2.4. Zetasizer analysis.** This method determined particle size, distribution, intensity-based dynamic light scattering (DLS), and zeta potentials of NPs were determined. DLS prepares a particle size measurement from scattered light within the solution. This analysis was performed in the stage of CPFX/ $\beta$ -CD, and that of CPFX/ $\beta$ -CD–CR, and the size of the particles was investigated (Fig. 3b). According to the obtained results, it is deduced that when the drug (CPFX) is loaded into the modified polymer structure ( $\beta$ -CD), the size of 96% of the particles is about 210 nm. The rest of the material is around 2  $\mu$ m (blue curve). Also, the polydispersity index (PDI) factor was 4.69, demonstrating particle accumulation. The 2.0  $\mu$ m size of particles may be due to the agglomeration of polymer material.

In the next stage, and after conjugating the synthesized dipeptide to the structure, the analysis was also done to check the particle size. It was seen that 77% of the particles are approximately 3.0  $\mu$ m and 20% of them are 600 nm (PDI = 2.93). It is likely that because of the agglomeration and hydrogen bond between dipeptide and polysaccharide structure, the size of the particles has grown larger. Zeta potential analysis is a crucial characterization approach to appraise the surface charge. Zeta potential (positive or negative) can influence the stability of particles and their cellular adhesion. The surface charge is caused by the physical interaction between the surface and particles. In this project, before conjugating the dipeptide, the ZETA potential was 13.7 mV; however, after the dipeptide conjugation, this amount increased to 14.7 mV.<sup>55</sup>

**2.2.5. XRD patterns.** X-ray powder diffraction spectroscopy can identify a complex's active ingredients and crystalline excipients. Fig. 4 shows that the complex does not have observable crystallization in the XRD results. The X-ray diffractogram of  $\beta$ -CD indicated peaks in the range of 10–15° and 15–20° ( $2\theta$ ) as well as the significant peaks at  $2\theta \approx 12^\circ$ , 18°, and 19°, which cause confirmation of the amorphous features of  $\beta$ -CD in nature.<sup>56</sup> Moreover, the CPFX influences the morphology of the previous structure, and a rise in peak intensity is observed referring to pure CPFX that shows the sharp peaks at  $2\theta = 14.4^\circ$ , 20.7°, 25.5° as well as the weak peaks at  $2\theta = 8.3^\circ$ , 13.4°, 16.5°.<sup>57</sup> As can be seen, some new weak peaks in the pattern of CPFX/ $\beta$ -CD–CR are attributed to the CR dipeptide on the surfaces.

**2.2.6. Electron microscopy imaging.** The field emission scanning electron microscope (FESEM) is utilized to investigate morphology (such as particle size and shape), metallographic details, uniformity, topology, and the investigation of elemental compositions. For the SEM sample preparation, we dispersed each sample in ethanol and sonicated them in a cleaner bath at an ambient temperature. A few amounts of the samples were poured on the glass laminate. As shown in Fig. 5, the size of

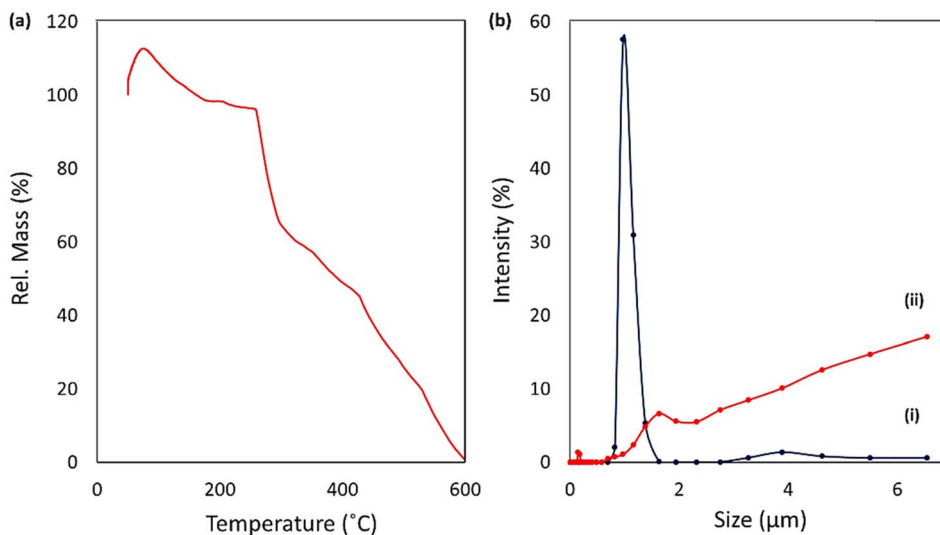


Fig. 3 (a) TGA curve of CPFX/ $\beta$ -CD–CR, and (b) intensity-based DLS curves of particle size (zeta-average) and size distribution of (i)  $\beta$ -CD–CR and (ii) CPFX/ $\beta$ -CD–CR nanocomplex.



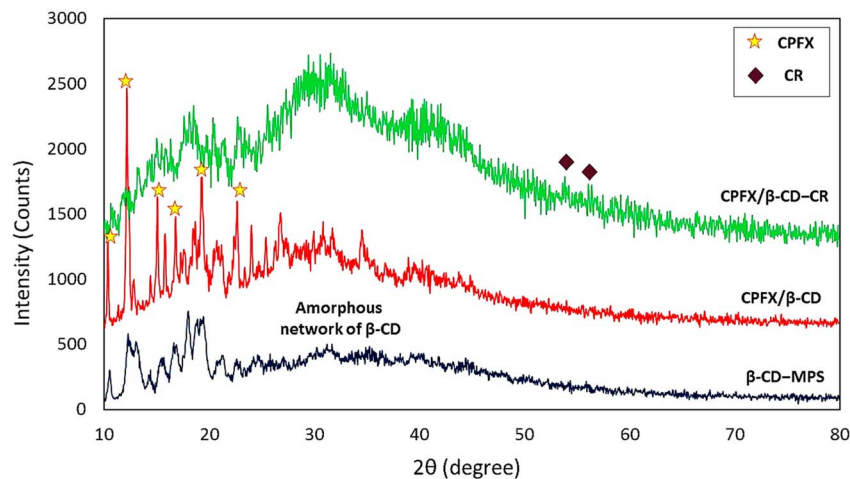


Fig. 4 XRD analysis of the  $\beta$ -CD-MPS, CPFX/ $\beta$ -CD-MPS, CPFX/ $\beta$ -CD-CR nanocomplex.

particles in pure  $\beta$ -CD is about 200 nm. In the case of modification of the polymer strands by MPS and further conjugation to CR dipeptide structure, the particle size has increased to 500 nm, while the uniformity is still confirmed. The final product demonstrates the rod morphology of particles with an average size of 1.0  $\mu$ m and high uniformity. The rods have more rapid enrichment and higher susceptibility; they also have the capability for major adhesion because of their high contact area. Rod-shaped particles can easily penetrate cells through the tip first. Nanorods with their main vertical axis tend to incorporate with the cell membrane. The rod-shaped nanoparticles achieved a superior targeting efficiency compared to other nanoparticle shapes like spherical, plate, or flake.<sup>58</sup> Consequently, based on these data, it can be claimed that the

designed nano-size cargo is suitably internalized into the target bacteria cells because the mean size and the general morphology of the particles are preferred in the cellular uptake process by the living cells.<sup>59</sup>

### 2.3. Antimicrobial properties of CPFX/ $\beta$ -CD-CR nanocomplex

The significant advantage of nanocarriers for targeted DDS is increasing the consistency of medicine and optimizing the half-life in blood serum.<sup>60</sup> The carriers decline side effects disturbance and boost drug resistance against degradation. Moreover, nanocarriers exhibit more therapy advantages with low dosages of drugs, and low doses of the drug delivery to the target cell

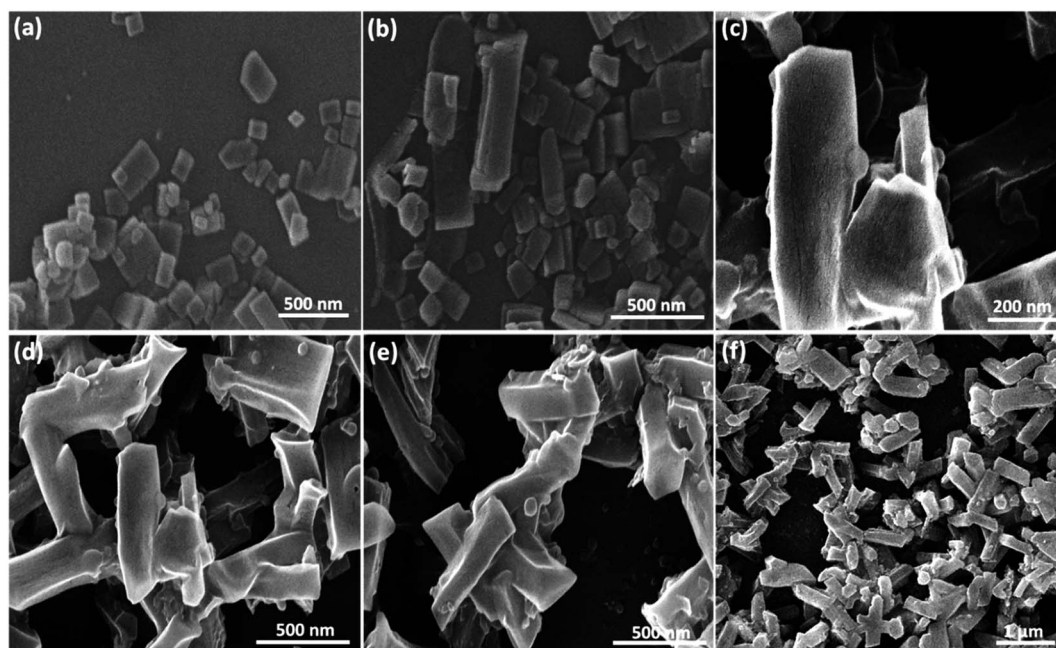


Fig. 5 FESEM images of (a) and (b)  $\beta$ -CD, (c) and (d)  $\beta$ -CD-MPS-CR, (e) and (f) CPFX/ $\beta$ -CD-CR nanocomplex.



could be faster and more controlled.<sup>64</sup> As mentioned in this literature,  $\beta$ -CD is ideal for drug delivery, and the drug loading mechanism improves cargo's bioavailability, solubility, and stability. Also, peptides are regarded as very effective and safe methods that do not damage the integrity of the cellular membrane. They can pass *via* different cell types of membranes. Some amino acids' attendance in forming the peptides, such as arginine, is crucial because it can interact with anionic sulfate or phosphate groups over the cell membrane. The MPTMS is the agent to create a disulfide bond between cysteine amino acids and can increase the antimicrobial effects. This study provided an efficient DDS construct from  $\beta$ -CD NPs covered by an MPTMS cross-linker to deliver the antibiotic CPFEX. Furthermore, a new dipeptide chain, which has been synthesized in the solid phase, was utilized as a more efficient factor for entering the bacteria cells and conjugating them to the structure.

**2.3.1. CPFEX loading in  $\beta$ -CD-CR.** Solid-state UV-vis diffuse reflectance spectroscopy (UV-DRS) was utilized to confirm the successful loading of CPFEX into the nanocarrier. As seen from the curves of Fig. 6, the  $\beta$ -CD spectrum indicates a UV reflectance activity in a wavelength range of 205–250 nm, including the sharp peaks at 211 and 225 nm. Also, the maximum reflectance by the neat CPFEX is situated in a range of 250–400 nm. Indeed, a noticeable reflectance activity for the CR-conjugated  $\beta$ -CD-MPS demonstrates successful attachment of CR onto the surfaces. Consequently, the final product has a considerable absorbance in a long range of 200–450 nm, confirming the CR conjugation and CPFEX loading into the structure.

**2.3.2. Release of CPFEX from CPFEX/ $\beta$ -CD-CR and drug content.** The food and drug administration (FDA) approved some approaches to specify the drug loading content (DLC) and drug loading efficiency (DLE), which will be mentioned below. *In vitro* condition, release studies were accomplished in acetate buffer (ACB 0.1 M, pH = 4.6) and phosphate buffer solutions (PBS 0.1 M, pH = 6.8 and 8.0) at 37 °C. Firstly, a calibration curve according to five standard solutions of CPFEX ( $\lambda_{\text{max}} = 276$  nm) with concentrations of 3, 5, 7, 9, and 13 ppm was acquired

(Fig. 7). The CPFEX release behavior was measured through UV-vis spectroscopy and compared with the calibration curve at different times (30, 60, 90, 180, 240, 300, and 360 minutes). Initially, the nanoparticles were centrifuged. Then, they were filtered with Whatman filter paper. Also, the blank sample was filtered with Whatman filter paper so as to eliminate the error related to the particulate matter of the paper filter. At last, the solution containing 5.0 mg of CPFEX was diluted for a correct UV-vis spectroscopy study. Afterwards, eqn (1) and (2) could be considered for all drug-loading content and release assessments. In the present study, the CPFEX loading efficiency in the CPFEX/ $\beta$ -CD-CR system was calculated to be 32.0%. According to Beer-Lambert principles, dilution of the sample is necessary to establish an accurate correlation between UV-vis (a.u.) and concentration (ppm). Hence, raw samples need 1/20 dilution with appropriate buffer media. Therefore, in acidic (optimum) conditions,  $A$  (UV-vis absorbance) was 1.203 (a.u.) for the sample after the drug release process. Afterwards,  $X$  which is the concentration of CPFEX (ppm), and  $C$  which is the concentration of the CPFEX solution ( $\text{mg mL}^{-1}$ ) were calculated *via* provided equations ( $X = 301$  ppm,  $C = 0.301$   $\text{mg mL}^{-1}$ ).<sup>45</sup>

$$X = (A + 0.001)/(0.0845 \times 0.05) \quad (1)$$

$$C = X \times 1/1000 \quad (2)$$

As can be seen, the maximum value of the released CPFEX has been shown in Table 1, which was regarded as the approximation of the CPFEX content (*ca.*  $30 \pm 0.2$ ) wt% in the CPFEX/ $\beta$ -CD-CR system. It can be deduced that inside the bacteria cell (following endocytosis), releasing the encapsulated CPFEX has occurred in the acidic condition, which is a foundation of the entire released quantity (100%), and the remaining extents were compared to this measure. As presented in Fig. 8, the maximum drug release of CPFEX from CPFEX/ $\beta$ -CD-CR nano-cargo occurred when the particles were dispersed in an acidic medium.

**2.3.3. Antimicrobial properties: zone of inhibition experiment.** To determine the antibacterial characteristics of the

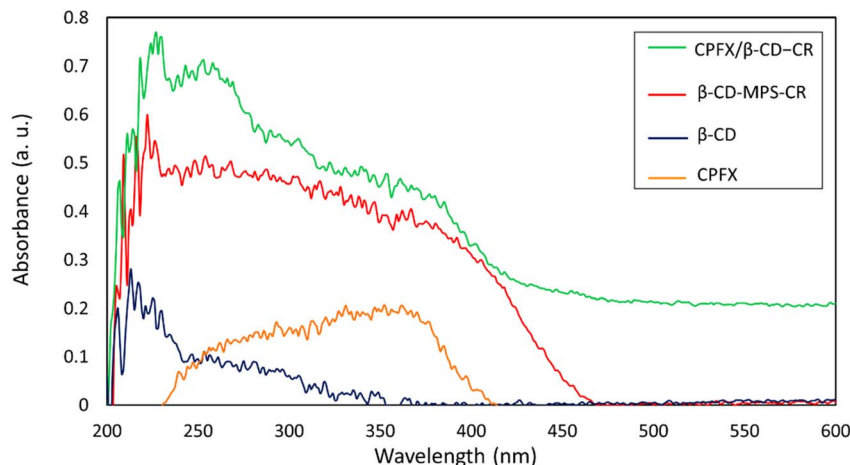


Fig. 6 UV-DRS spectra of the neat  $\beta$ -CD, CPFEX,  $\beta$ -CD-MPS-CR, and CPFEX/ $\beta$ -CD-CR nanocomplex.



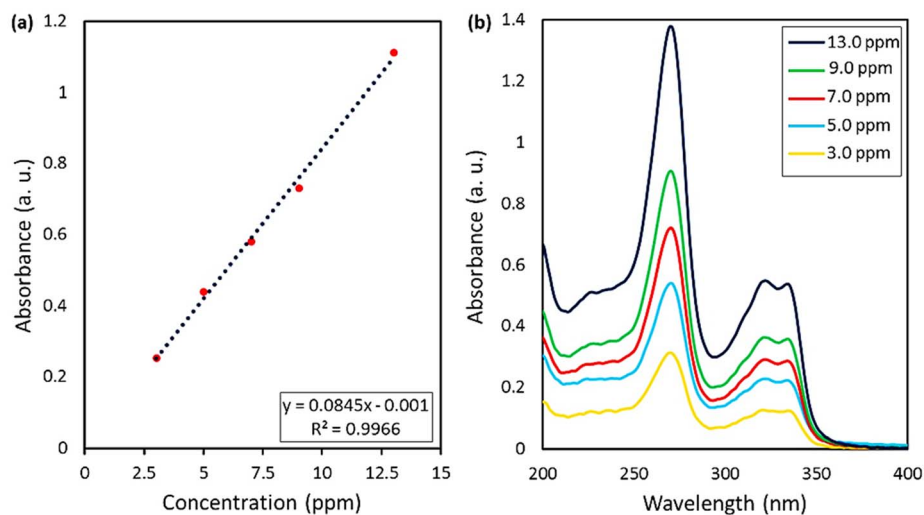


Fig. 7 (a) Calibration curve of the standard CPFV solutions, obtained by UV-vis spectrophotometry, (b) UV-vis spectra of CPFV at various concentration values.

Table 1 CPFV-release data for CPFV/ $\beta$ -CD-CR nanocomplex under different conditions

Entry	Condition <sup>a</sup>	Absorbance (a.u.)	Concentration (mg mL <sup>-1</sup> )	CPFV release (%)	Rel. E <sup>b</sup> (%)
1	ACB (0.1 M, pH = 4.6)	1.203	0.301	100 <sup>c</sup>	3.5
2	PBS (0.1 M, pH = 6.8)	0.416	0.104	34.55	5.2
3	PBS (0.1 M, pH = 8.0)	0.924	0.231	76.74	4.6

<sup>a</sup> CPFV release was investigated at 37 °C and 4 h. <sup>b</sup> % Rel. E: relative error percentage for three identical samples. <sup>c</sup> Complete value of release (100%) was considered for most of the drugs released, and the remaining values were compared to the main value.

CPFV/ $\beta$ -CD-CR therapeutic nano-bioconjugate, the growth rate of two bacterial strains, for example, *S. aureus* and *E. coli*, was investigated according to the presence of the control via the ZOI test.<sup>62,63</sup> *S. aureus* and *E. coli* were selected as Gram-positive and Gram-negative bacteria with different surface characteristics, respectively. Features such as cell adhesion to solid surfaces and flocculation strongly depend on surface properties, surface electrical connections, and surface hydrophobicity. The outer cell membrane of Gram-negative bacteria, including *Escherichia coli* (*E. coli*), is covered with a lipopolysaccharide layer of 1–3 pm thickness. Whereas the surface of Gram-positive bacteria such as *Staphylococcus aureus* (*S. aureus*) has a peptidoglycan layer that teichuronic acid, teichoic acid, and proteins are covalently attached to it. For this reason, there is a significant difference in the electrophoretic behavior of the two bacteria, which leads to a significant difference in the surface properties between the two types of bacteria. So, they were selected as two common Gram-positive and Gram-negative bacteria in this research.<sup>64</sup>

This assay tested similar dosages of CPFV/ $\beta$ -CD-CR,  $\beta$ -CD, CR, and CPFV. The powdery water-undissolved samples were situated on the agar plates containing bacterial cells. In this regard, 2.0 mg of powder samples were transformed onto agar gels containing *S. aureus* and *E. coli*. The disks were incubated at 37 °C, with a humidity of 95% for 24 h. After incubation, the inhibition zone diameter was measured. Fig. 9a displays that

the ZOI of *E. coli* was larger than *S. aureus*, which is attributed to the CPFV/ $\beta$ -CD-CR therapeutic nano-bioconjugate. The growth zone inhibitory of CPFV/ $\beta$ -CD-CR particles on the *E. coli* and the *S. aureus* bacterial cells was  $5.5 \pm 0.2$  cm and  $3.5 \pm 0.2$  cm, respectively.

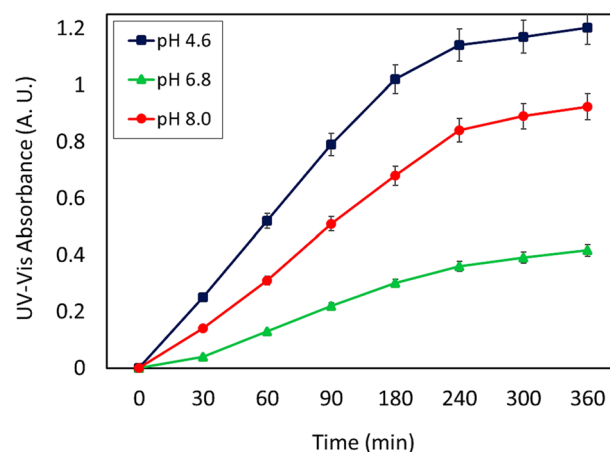


Fig. 8 The release profile of CPFV from CPFV/ $\beta$ -CD-CR nano-cargo in three different buffered conditions ACB (0.1 M, pH = 4.6), PBS (0.1 M, pH = 6.8) and PBS (0.1 M, pH = 8.0) [the errors ( $\pm$ ) represent the relative error values in each case ( $n = 3$ )].



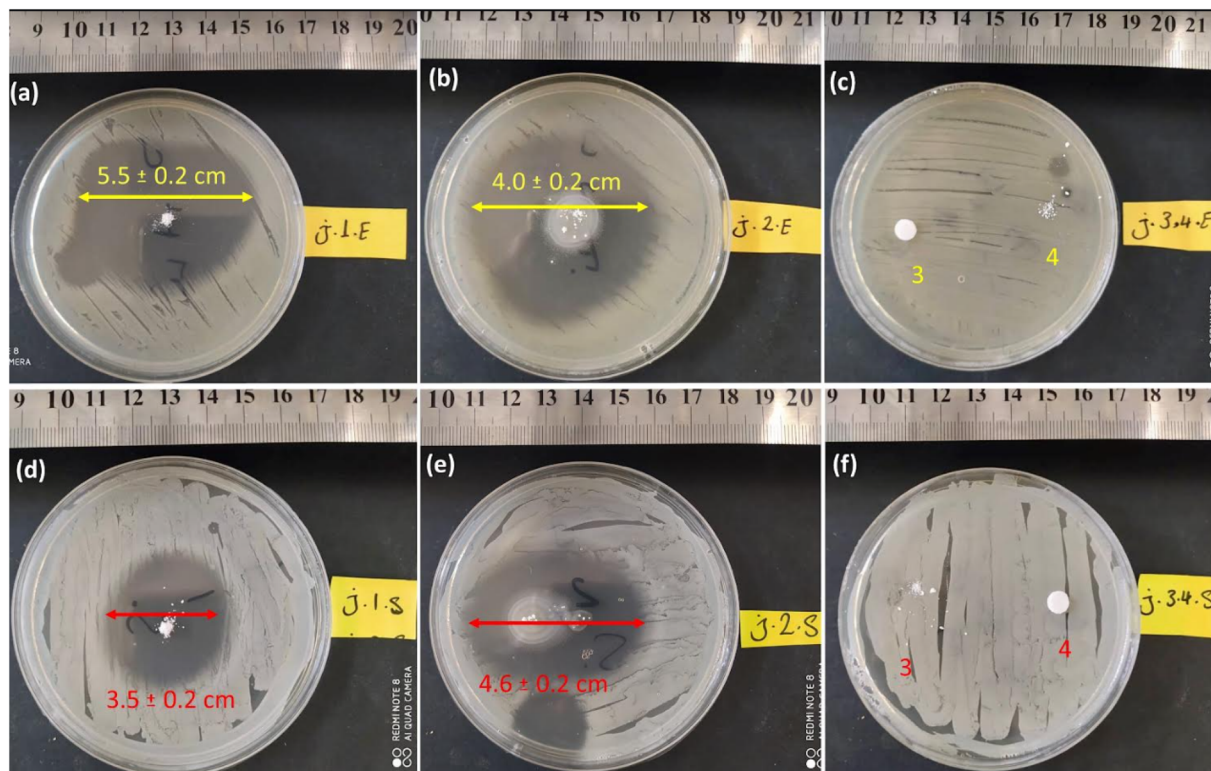


Fig. 9 Digital photos of the growth-inhibition zones created by CPFX/β-CD-CR nano-cargo, dipeptide sequence, and individual CPFX (with an equal dosage: 2.0 mg), on *E. coli* (a)–(c) and *S. aureus* (d)–(f) cell lines [errors (±) represent absolute errors per three repeated samples ( $n = 3$ )]. (a) CPFX/β-CD-CR (nano-cargo), (b) CPFX (drug), (c) β-CD (3), CR (4) on *E. coli*, (d) CPFX/β-CD-CR, (e) CPFX, (f) β-CD (3), CR (4) on *S. aureus* strain.

In contrast, as shown in Fig. 9b, the ZOI measurements for the individual CPFX on the *E. coli* were reduced to  $4.0 \pm 0.2$  cm. Concludingly, the CPFX/β-CD-CR therapeutic nano-bioconjugate with about 30% drug content has higher antibacterial activity than the individual CPFX with the same dosage. Significantly, due to the thicker, strong walls of Gram-negative *E. coli* bacteria, CPFX hardly penetrates the membrane; hence, the ZOI of the *E.*

*coli* samples is larger than in the case of *S. aureus*. In addition, the dipeptide sequence and polymer effects on the ZOI test have been evaluated. In this respect, the individual dipeptide and polymer did not demonstrate the ZOI onto *S. aureus* and *E. coli* cell lines, indicating no antibacterial activity of the dipeptide and polymer (Fig. 9c and f).

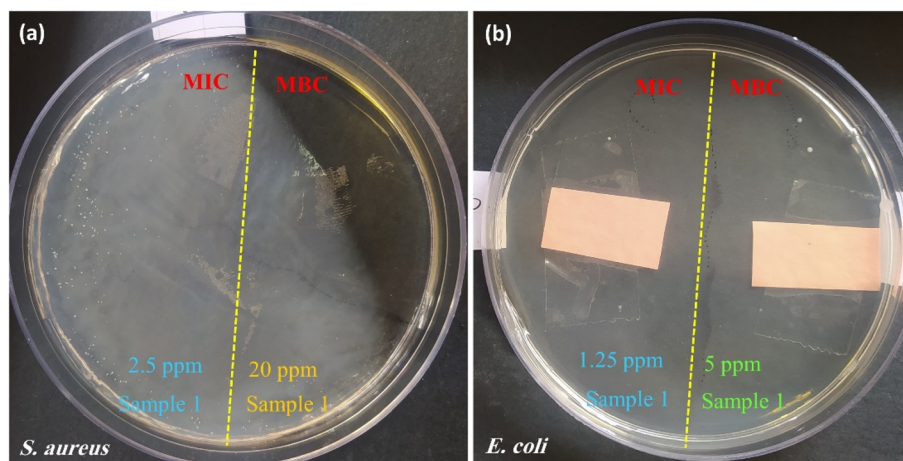


Fig. 10 Digital photos of MIC/MBC disks containing (a) CPFX/β-CD-CR nano-cargo in *S. aureus* (MIC =  $2.5 \mu\text{g mL}^{-1}$  and MBC =  $20 \mu\text{g mL}^{-1}$ ), and (b) CPFX/β-CD-CR nano-cargo (with an equal dosage: 2.0 mg) onto *E. coli* cell lines (MIC =  $1.25 \mu\text{g mL}^{-1}$  and MBC =  $5 \mu\text{g mL}^{-1}$ ) incubated 48 hours at  $37^\circ\text{C}$  and a humidity of 95%.



**Table 2** The MIC and MBC values for the prepared CPF<sub>2</sub>X/β-CD–CR therapeutic nano bioconjugate and CPF<sub>2</sub>X as a standard

Bacterial strain	Sample 1 (CPF <sub>2</sub> X/β-CD–CR)	Sample 2 (ciprofloxacin)
<i>S. aureus</i>	MIC (μg mL <sup>-1</sup> ): 2.5 MBC (μg mL <sup>-1</sup> ): 20.0	MIC (μg mL <sup>-1</sup> ): 0.5 MBC (μg mL <sup>-1</sup> ): 2.0
<i>E. coli</i>	MIC (μg mL <sup>-1</sup> ): 1.25 MBC (μg mL <sup>-1</sup> ): 5.0	MIC (μg mL <sup>-1</sup> ): 0.02 MBC (μg mL <sup>-1</sup> ): 0.04

**2.3.4. Determination of minimum inhibitory and bactericidal concentrations. The minimum inhibitory concentration (MIC) and the minimum bactericidal concentration (MBC).** Due to the results of the ZOI experiment, the MIC/MBC and colony count approaches were accomplished for CPF<sub>2</sub>X/β-CD–CR therapeutic nano-bioconjugate and individual CPF<sub>2</sub>X on *S. aureus* and *E. coli*. For MIC/MBC experiment, a dilution series was prepared in a sterile test tube.<sup>65</sup> First, the amount of the CPF<sub>2</sub>X/β-CD–CR particles have been dispersed in deionized water. Afterwards, 10 solutions were made *via* dilution of Mueller–Hinton broth (labeled 1 to 8). The first tube was labeled as C–, indicating CPF<sub>2</sub>X/β-CD–CR control, and the final tube was labeled as C+, showing the growth control. Then, 1.0 mL of Mueller–Hinton broth was injected into each tube, and 1.0 mL of the CPF<sub>2</sub>X/β-CD–CR mixture was poured into tubes No. 1 and C–. Next, 1.0 mL of tube No. 1 contents were conveyed into tube No. 2. After pipetting the contents of tube No. 2, 1.0 mL of its content was moved to tube No. 3, and so on. This process was followed to tube No. 8. The C– labeled tube was applied as CPF<sub>2</sub>X/β-CD–CR control, and the last C+ labeled tube was used as growth control, receiving no antibacterial agents. Next, the microplate was exposed to incubation with 1.0 mL of the culture of *S. aureus* and *E. coli*. Then, the microplate was incubated under similar conditions for 24 h. At last, the microplate was tested for bacterial growth, and the MIC/MBC contents were assessed for the CPF<sub>2</sub>X/β-CD–CR therapeutic nano-bioconjugates (Fig. 10). The MIC/MBC assay data is represented in Table 2.

Further assessments on the antibacterial characteristics of the CPF<sub>2</sub>X/β-CD–CR therapeutic nano-bioconjugates were accomplished through the colony count assay.<sup>66</sup> In this account, the linear cell culture pattern was implemented on the agar gel. Then, the sample was spread throughout the disks and incubated at 37 °C, with 95% humidity for 48 h. The results revealed that the *S. aureus* population on the CPF<sub>2</sub>X/β-CD–CR therapeutic nano-bioconjugates-containing disk after 30, 60 and 180 minutes was 250.0, 150.0 and 5.0 (×10<sup>8</sup> CFU mL<sup>-1</sup>), respectively, and *E. coli* bacteria population on the CPF<sub>2</sub>X/β-CD–CR therapeutic nano-bioconjugates-containing disk during those times was 10.0, 5.0 and diminished to zero. Notably, the CPF<sub>2</sub>X/β-CD–CR nano-cargo's cell-killing activity with about 30% drug content was analogous to the individual CPF<sub>2</sub>X with a similar concentration. As expected, no bacterial population difference was seen between the control sample and the CR-containing disk.

**Table 3** The brand and purity of the utilized chemicals in this study

Materials	Brand & purity
Beta cyclodextrin	Sigma-Aldrich
(3-Mercaptopropyl)trimethoxy silane (MPTMS)	Sigma-Aldrich, 97.0%
Ciprofloxacin	Sigma-Aldrich
<i>N,N,N',N'</i> -Tetramethyl- <i>O</i> -(benzotriazol-1-yl)uranium tetrafluoroborate (TBTU)	Sigma-Aldrich, ≥97.0%
Fmoc-Arg(Pbf)-OH	Sigma-Aldrich, ≥98.0%
Fmoc-Cys(Trt)-OH	Sigma-Aldrich, ≥95.0%
2-Chlorotriethyl chloride (CTC) resin	Sigma-Aldrich, 97.0%
<i>N,N</i> -Diisopropylethylamine (DIPEA)	Sigma-Aldrich, ≥99.0%
<i>N,N</i> -Dimethylformamide (DMF)	Sigma-Aldrich, 99.8%
Dichloromethane (DCM)	Sigma-Aldrich, 99.9%
Piperidine	Sigma-Aldrich, ≥99.0%
Trifluoroacetic acid (TFA)	Sigma-Aldrich, ≥99.0%
Synthetic ethanol	Merck, 99%
Synthetic methanol	Merck, 99%

**Table 4** The brand and model of the used devices in this study

Equipment	Brand
FT-IR spectroscopy	Shimadzu FT-IR-8400S
EDX spectroscopy	VEGA-TESCAN-XMU
TGA analysis	Bahr-STA 504
DLS analysis	Horiba (SZ-100)
XRD	DRON-8 X-ray diffractometer
FESEM	Zeiss Sigma
Solid state	Shimadzu-UV-2550/220v
UV-vis spectroscopy	
UV-vis spectroscopy	Beckman DU640
Ultrasonic cleaner bath	BANDELIN electronic GmbH & Co. KG
Centrifuge	Beckman Coulter GmbH
Oven	Genlab Ltd
Freeze drier	KASSEL Machinery (Zhejiang) Co., Ltd
Rotary evaporator	Heidolph Instruments GmbH & Co. KG
Incubator	Sh, Noor Sanat Ferdos
Shaker	VWR 5000
Autoclave (for sterilization)	Reyhan Teb, 2KW-220v
Vacuum pump	Heidolph persia LQ1

## 3. Experimental section

### 3.1. Materials and instruments

All chemicals and devices utilized in this study are listed in Tables 3 and 4.

### 3.2. Preparation methods

**3.2.1. Modification of β-CD by MPS.** There are some steps to functionalize the structure of the polymer: first, the dissolution of precursor 1.0 g β-CD into 20.0 mL distilled water. Next, 15.0 mL MPTMS was dissolved into the 10.0 mL ethanol, and then the mixture was added to the above precursor solution, followed by subsequent ultrasonic treatment for 10 min. Afterwards, the mixture was conveyed into a 50.0 mL round-bottom flask and refluxed at 80 °C for 48 h under vigorous stirring



conditions. Then through the rotary device, the solvents separated, and the collected product was washed with ethanol (10.0 mL  $\times$  3) and water (10.0 mL  $\times$  3). Finally, the white product was separated from the solution by centrifugation at 9k rpm for 10 min, and the resulting particles were dried for 12 h in an oven at 60 °C.

**3.2.2. Synthesis of CR dipeptide compound in the solid phase.** For this purpose, CTC (0.8 mmol  $g^{-1}$ ) resin (1.0 g) was washed with DMF and DCM (10.0 mL). Afterwards, *via* DIEA, the first amino acid [Fmoc-Cys(Trt)-OH] (1.0 mmol) was connected to the resin. Next, the capping step was carried out *via* methanol solution; subsequently, the protection group of Fmoc was eliminated with a piperidine solution in the DMF (25%). Next, the mixture of HBTU (1.0 mmol) and DIEA in DMF (5.0 mL) and second amino acid [Fmoc-Arg(pbf)-OH] (0.8 mmol) has been attached. TFA (95%) is used for the last deprotection and separation of the CR dipeptide complex from the CTC. All the process was fulfilled based on the detailed information from the synthesis of the peptide method in our previous works. The structure and purity of the synthesized CR dipeptide have been approved by H-NMR spectroscopy, as given in our previous report.<sup>46</sup>

**3.2.3. Conjugation of the  $\beta$ -CD-MPS particles with the synthesized CR dipeptide.** In a round-bottom flask (50.0 mL),  $\beta$ -CD-MPS (0.1 g) was dispersed in a solution of H<sub>2</sub>O<sub>2</sub> (35.0%, 1.0 mL) *via* an ultrasonic ice bath for 10 minutes at 10 °C temperature. After that, the CR dipeptide complex (0.05 g) was added to the flask *via* the drop-by-drop method (dissolved in ethanol). Then, the combination was stirred at 10 °C for 2 h. In the end, the CPF<sub>X</sub>/ $\beta$ -CD-CR particles were collected by centrifuge (15 min, 4k rpm). Consequently, the particles were dried with a freeze dryer for 48 h.

**3.2.4. CPF<sub>X</sub> loading into  $\beta$ -CD-CR.** In this regard, in a glass tube (13  $\times$  100 mm),  $\beta$ -CD-MPS (0.5 g) were dispersed in a provided solution of CPF<sub>X</sub> (0.1 M) in ethanol (3.0 mL) and DI water (3.0 mL) for 10 min *via* ultrasonic cleaner bath. Next, the combination was stirred in a dark room at 25 °C for 6 h. Finally, the particles were collected by centrifuge (15 min, 4k rpm) and twice rinsed with ethanol to eliminate the adsorbed CPF<sub>X</sub> over the surfaces. Then the particles were redispersed in deionized water and dried with a freeze dryer for 48 h.

### 3.3. Cellular experiments

**3.3.1. Cell cultivation.** Initially, the incubation of *S. aureus* and *E. coli* bacterial strains was carried out on Mueller–Hinton agar gel in Petri dishes for 24 h. After that, the 0.5 McFarland solution was prepared using the following process: barium chloride (0.5%) was added to sulfuric acid (0.36 N). The similarity in the opacity of the solution with bacterial cells in the physiological serum with standard solution indicates 1.0–1.5  $\times$  10<sup>8</sup> CFU mL<sup>-1</sup> concentration.<sup>67</sup> These bacteria cells were situated on the agar gel with cotton swabs and incubated at 37.0  $\pm$  1.0 °C with a humidity of 95% for 24 h.

**3.3.2. ZOI experiments.** First, swabs impregnated the Mueller–Hinton agar gel dishes with bacterial cells. Next, the CPF<sub>X</sub>,  $\beta$ -CD, CR, and CPF<sub>X</sub>/ $\beta$ -CD-CR samples were prepared to

evaluate the antibacterial activity of the CPF<sub>X</sub>/ $\beta$ -CD-CR. Then, 5.0 mg of the powder sample was used to put 5.0 mg mL<sup>-1</sup> of the samples on the agar gel when there were water-undissolved samples. Finally, a cell-impregnated disk was concentratedly placed on the agar gel when there were solution samples. The plate was incubated at 37 °C, with 95% humidity, for 24 h.

**3.3.3. MIC/MBC and colony count experiments.** MIC indicates the minimum antibacterial agent required to prevent turbidity due to the bacteria growth in the liquid bacterial culture medium.<sup>68</sup> The standard Mueller–Hinton broth dilution approach was applied to assess the CPF<sub>X</sub>/ $\beta$ -CD-CR therapeutic nano bioconjugate antibacterial effect by considering the growth of apparent bacteria in the agar broth. For example, the bacterial strains *S. aureus* and *E. coli* were initially incubated at 37 °C. The inoculated broth-containing control was incubated at 37 °C for 24 h. Next, the samples' inhibition effect was evaluated *via* a modified microdilution approach to clarify their MIC values. Therefore, dilution series in 2.0 mL of Mueller–Hinton broth liquid medium was prepared with pure and 0.039, 0.078, 0.156, 0.3125, 0.625, 1.25, 2.5, 5.0, 10.0, and 20.0  $\mu$ g mL<sup>-1</sup> concentrations followed by a bacterial suspension with 0.5 McFarland turbidity. After that, the McFarland standard (10<sup>8</sup>  $\times$  1.5 CFU mL<sup>-1</sup>) was added to the content of 20  $\mu$ L in each well. Consequently, the microplate was incubated at 37 °C for 24 h, and the MIC results were considered and inquired. MIC referred to the lowest concentration of the CPF<sub>X</sub>/ $\beta$ -CD-CR therapeutic nano bioconjugate, where no bacterial growth was observed. In addition, MBC is defined as the antibacterial agent's minimum concentration, which reduces the minimum number of bacteria after 24 h to *ca.* 0.001 of the bacteria number at the starting time (*t*<sub>0</sub>). The MBC and MIC determination methods are almost similar; however, the successive dilution procedure was employed for counting the bacteria from the MIC wells concentration upward. The minimum values of MIC and MBC are attributed to the CPF<sub>X</sub>/ $\beta$ -CD-CR therapeutic nano-bioconjugate onto *S. aureus* and *E. coli* bacteria compared to the individual CPF<sub>X</sub>. The linear cell culture pattern of *S. aureus* and *E. coli* was made by sterilized inoculation loops on the agar gel, and their colony was spread all over the gel.<sup>69</sup> Afterward, the sample drop was placed on the disk gel and distributed by an L-shaped glass. This plate was incubated at 37 °C with 95% humidity for 48 h.

### 3.4. Sample preparation for characterization

For electron microscopy, the particles were dispersed in minimum amount of pure ethanol, and ultrasonicated with a cleaner bath (50 kHz, 100 W L<sup>-1</sup>) for 5 min, at an ambient temperature. Afterward, 50  $\mu$ L of each sample was poured onto a glass laminate, dried in vacuum oven, and then sent to the SEM imaging laboratory. The same procedure was followed for the biological tests, with the difference that the environment in which the whole sample was dispersed in was DMEM instead of ethanol, and the temperature was maintained in a range of 0–5 degrees Celsius (ice bath). The samples were maintained on ice and subjected to living cells in an incubator. For the UV-vis studies, the nanoparticles were dispersed in buffered media,



stirred, and finally centrifuged (20 000 rpm, 10 min) to collect the carrier coils. Then, they were filtered with a Whatman filter paper. Also, the blank sample was filtered with Whatman filter paper so as to eliminate the error related to the particulate matter of the paper filter. At last, the solution containing 5.0 mg of CPFY was diluted for a correct UV-vis spectroscopy study.

## 4. Conclusions

We designed a novel DDS which is a complex of nanoscale  $\beta$ -CD with CPFY conjugated to a cell adhesive dipeptide (CR). The nanocomplex's biological activities *versus* Gram-positive (*S. aureus*) and Gram-negative (*E. coli*) bacteria were studied. The surface of  $\beta$ -CD was initially modified with MPTMS to introduce –SH groups onto the surface to provide this biocompatible DDS. In addition, the CPFY was loaded to the nanoscale  $\beta$ -CD, and finally, *via* the formation of a disulfide bond, the synthesized CR dipeptide is linked to the surfaces of CPFY/ $\beta$ -CD cargo. This dipeptide sequence was synthesized in the solid phase on CTC resin with high purity. The peptide structures are highly effective, safe techniques and can penetrate cells non-invasive. Also, the usage of this novel-designed strategy prepared a plethora of benefits compared to the usage of free CPFY for bacterial growth prohibition. The primary benefit was using lower doses of antibiotics for similar therapeutic effects. Herein, every essential characterization, including; FT-IR, EDX, TGA, zeta potential, UV-DRS, XRD, FESEM and UV-vis absorbance, was accomplished the received results confirmed with the designed structure.

Furthermore, the drug content and release were investigated with precise analytical methods. The drug loading efficacy was 32%, and the main release was revealed in an acidic environment. Overall, according to the antimicrobial results, it can be deduced that the efficacy of the CPFY is remarkably gained *via* the complexation of nanoscale materials and engineered dipeptides. The growth zone inhibitory of CPFY/ $\beta$ -CD–CR particles on the *E. coli* and the *S. aureus* bacterial cells was  $5.5 \pm 0.2$  cm and  $3.5 \pm 0.2$  cm, respectively. Moreover, the half-life of the provided cargo related to the degradability of the used components in the system ought to be assessed. Following complete degradation, the magnitude of released components' toxicity may be another significant challenge.

## Author contributions

Reza Taheri-Ledari: conceptualization, reviewing, and editing of the main draft, supervision and project administration, and software; Farinaz Jalali: performed all practical sections and also in preparation of the initial draft; Leili Heidari: performed all antimicrobial sections and interpreted the obtained results; Fatemeh Ganjali: wrote the initial draft and interpreted the obtained results; Fereshteh Rasouli Asl: participated in partial parts of the bench work and also in preparation of the initial draft; Simindokht Zarei-Shokat: participated in partial parts of the bench work; Mohadeseh Forouzandeh-Malati: graphics and software; Adibeh Mohammadi: participated in the revision stage; Ali Maleki: managed all sections of the work, supervision, project administration, and financial support.

## Funding

This work was partially supported by the Iran University of Science and Technology.

## Conflicts of interest

The authors declare no competing financial interest.

## Acknowledgements

The authors acknowledge the partial support from the Research Council of the Iran University of Science and Technology (IUST).

## References

- 1 V. Soltaninejad, M. R. Ahghari, R. Taheri-Ledari and A. Maleki, *Langmuir*, 2021, **37**, 4700–4713.
- 2 M. Tian, X. He, Y. Feng, W. Wang, H. Chen, M. Gong, D. Liu, J. L. Clarke and A. van Eerde, *Antibiotics*, 2021, **10**, 539.
- 3 A. Maleki, R. Taheri-Ledari, R. Eivazzadeh-Keihan, M. de la Guardia and A. Mokhtarzadeh, *Curr. Org. Synth.*, 2019, **16**, 765–771.
- 4 K. Drlica and X. Zhao, *Expert Rev. Anti-Infect. Ther.*, 2021, **19**, 601–618.
- 5 W. Duan, H. Cui, X. Jia and X. Huang, *Sci. Total Environ.*, 2022, 153178.
- 6 T. D. Pham, Z. M. Ziora and M. A. Blaskovich, *Medchemcomm*, 2019, **10**, 1719–1739.
- 7 M. Vidyavathi and G. Srividya, *Int. J. Appl. Pharm.*, 2018, **10**, 6.
- 8 A. K. Al-Buriahi, M. M. Al-shaibani, R. M. S. R. Mohamed, A. A. Al-Gheethi, A. Sharma and N. Ismail, *Journal of Water Process Engineering*, 2022, **47**, 102725.
- 9 G.-F. Zhang, X. Liu, S. Zhang, B. Pan and M.-L. Liu, *Eur. J. Med. Chem.*, 2018, **146**, 599–612.
- 10 A. Rehman, W. M. Patrick and I. L. Lamont, *J. Med. Microbiol.*, 2019, **68**, 1–10.
- 11 R. Taheri-Ledari, W. Zhang, M. Radmanesh, S. S. Mirmohammadi, A. Maleki, N. Cathcart and V. Kitaev, *Small*, 2020, **16**, 2002733.
- 12 R. Taheri-Ledari, W. Zhang, M. Radmanesh, N. Cathcart, A. Maleki and V. Kitaev, *J. Nanobiotechnol.*, 2021, **19**, 239.
- 13 A. Patil, V. Mishra, S. Thakur, B. Riyaz, A. Kaur, R. Khurshid, K. Patil and B. Sathe, *Curr. Nanosci.*, 2019, **15**, 137–146.
- 14 Z. A. Bhutta, M. Shoaib, A. Kanwal, A. Ashar, A. Mahfooz, R. Ahmed, M. Ali, M. F.-e.-A. Kulyar and K. Li, in *Advancements in Controlled Drug Delivery Systems*, IGI Global, 2022, pp. 97–133.
- 15 R. Taheri-Ledari, E. Zolfaghari, S. Zarei-Shokat, A. Kashtiaray and A. Maleki, *Commun. Biol.*, 2022, **5**, 995.
- 16 H. Lu, J. Wang, T. Wang, J. Zhong, Y. Bao and H. Hao, *J. Nanomater.*, 2016, **2016**, 5762431.
- 17 W. Zhang, R. Taheri-Ledari, F. Ganjali, *et al.*, *Heliyon*, 2022, **8**, e09577.
- 18 R. Taheri-Ledari, in *Heterogeneous Micro and Nanoscale Composites for the Catalysis of Organic Reactions*,



- Classification of micro and nanoscale composites, Elsevier, 2022, pp. 1–21.
- 19 R. Taheri-Ledari, M. Saeidirad, F. S. Qazi, A. Fazeli, A. Maleki and A. E. Shalan, *RSC Adv.*, 2021, **11**, 25284–25295.
- 20 R. Taheri-Ledari, J. Rahimi, A. Maleki and A. E. Shalan, *New J. Chem.*, 2020, **44**, 19827–19835.
- 21 A. Maleki, R. Taheri-Ledari and M. Soroushnejad, *ChemistrySelect*, 2018, **3**, 13057–13062.
- 22 R. Kore, A. D. Sawant and R. D. Rogers, *ACS Sustainable Chem. Eng.*, 2021, **9**, 8797–8802.
- 23 R. Taheri-Ledari, J. Rahimi and A. Maleki, *Ultrason. Sonochem.*, 2019, **59**, 104737.
- 24 R. Taheri-Ledari, S. S. Mirmohammadi, K. Valadi, A. Maleki and A. E. Shalan, *RSC Adv.*, 2020, **10**, 43670–43681.
- 25 R. Taheri-Ledari and A. Maleki, *New J. Chem.*, 2021, **45**, 4135–4146.
- 26 W. Zhang, R. Taheri-Ledari, F. Ganjali, F. H. Afruzi, Z. Hajizadeh, M. Saeidirad, F. S. Qazi, A. Kashtiaray, S. S. Sehat and M. R. Hamblin, *Heliyon*, 2022, e09577.
- 27 F. Ganjali, A. Kashtiaray, S. Zarei-Shokat, R. Taheri-Ledari and A. Maleki, *Nanoscale Adv.*, 2022, **4**, 1263–1307.
- 28 R. Taheri-Ledari, K. Valadi, S. Gharibi and A. Maleki, *Mater. Res. Bull.*, 2020, **130**, 110946.
- 29 R. Taheri-Ledari and A. Maleki, in *Magnetic Nanoparticle-Based Hybrid Materials*, Elsevier, 2021, pp. 619–636.
- 30 X. Zhang, Z. Chen, X. Liu, S. L. Hanna, X. Wang, R. Taheri-Ledari, A. Maleki, P. Li and O. K. Farha, *Chem. Soc. Rev.*, 2020, **49**, 7406–7427.
- 31 Z. Hajizadeh, K. Valadi, R. Taheri-Ledari and A. Maleki, *ChemistrySelect*, 2020, **5**, 2441–2448.
- 32 R. Taheri-Ledari, K. Valadi and A. Maleki, *Prog. Photovoltaics*, 2020, **28**, 956–970.
- 33 K. Valadi, S. Gharibi, R. Taheri-Ledari, S. Akin, A. Maleki and A. E. Shalan, *Environ. Chem. Lett.*, 2021, **19**, 2185–2207.
- 34 A. Banerjee, J. Qi, R. Gogoi, J. Wong and S. Mitragotri, *J. Controlled Release*, 2016, **238**, 176–185.
- 35 K. E. Bremmell and C. A. Prestidge, *Drug Dev. Ind. Pharm.*, 2019, **45**, 349–358.
- 36 I.-H. Cho, D. H. Kim and S. Park, *Biomater. Res.*, 2020, **24**, 1–12.
- 37 G. Crini, S. Fourmentin, É. Fenyvesi, G. Torri, M. Fourmentin and N. Morin-Crini, *Environ. Chem. Lett.*, 2018, **16**, 1361–1375.
- 38 V. J. Stella and R. A. Rajewski, *Int. J. Pharm.*, 2020, **583**, 119396.
- 39 T. Jia, S. Huang, C. Yang and M. Wang, *Mol. Pharm.*, 2017, **14**, 2529–2537.
- 40 W. Kauffman, S. Guha and W. C. Wimley, *Nat. Commun.*, 2018, **9**, 1–10.
- 41 C. Bechara and S. Sagan, *FEBS Lett.*, 2013, **587**, 1693–1702.
- 42 B. Khan, S. Kumar, N. Sanbhal, S. Abdullah, J. Hussain, N. Chowdhry, A. Q. Ansari and M. M. Surahio, *Biomed. Mater. Devices*, 2022, 1–12.
- 43 R. Jelić, M. Tomović, S. Stojanović, L. Joksović, I. Jakovljević and P. Djurdjević, *Monatsh. Chem.*, 2015, **146**, 1621–1630.
- 44 W. Zhang, R. Taheri-Ledari, Z. Hajizadeh, E. Zolfaghari, M. R. Ahghari, A. Maleki, M. R. Hamblin and Y. Tian, *Nanoscale*, 2020, **12**, 3855–3870.
- 45 Z. Aytac, S. Ipek, I. Erol, E. Durgun and T. Uyar, *Colloids Surf., B*, 2019, **178**, 129–136.
- 46 R. Taheri-Ledari, A. Fazeli, A. Kashtiaray, S. Salek Soltani, A. Maleki and W. Zhang, *Langmuir*, 2021, **38**, 132–146.
- 47 R. Xu, X. Lin, J. Xu and C. Lei, *Ionics*, 2020, **26**, 3359–3365.
- 48 M. Hezarjaribi, G. Bakeri, M. Sillanpää, M. J. Chaichi, S. Akbari and A. Rahimpour, *Environ. Sci. Pollut. Res.*, 2021, **28**, 51808–51825.
- 49 R. Nithya and N. Meenakshi Sundaram, *Int. J. Nanomed.*, 2015, **10**, 119–127.
- 50 B. A. Mohamed and P. Janaki, *J. Appl. Nat. Sci.*, 2021, **13**, 110–123.
- 51 H. Sadaquat and M. Akhtar, *J. Inclusion Phenom. Macrocyclic Chem.*, 2020, **96**, 333–351.
- 52 M. Sajid, M. Asif, N. Baig, M. Kabeer, I. Ihsanullah and A. W. Mohammad, *Journal of Water Process Engineering*, 2022, **47**, 102815.
- 53 H. Butt, M. U. Minhas, K. U. Khan, M. Sohail, I. Khalid, S. Rehmani and M. Suhail, *Polym. Bull.*, 2022, 1–22.
- 54 M. Zarif, A. Afidah, J. Abdullah and A. Shariza, *Biomed. Res.*, 2012, **23**, 513–520.
- 55 J. Souri, H. Almasi, H. Hamishehkar and S. Amjadi, *Lwt*, 2021, **151**, 112174.
- 56 J. Chen, X. Qin, S. Zhong, S. Chen, W. Su and Y. Liu, *Molecules*, 2018, **23**, 1179.
- 57 D. Macocinschi, D. Filip, S. Vlad, C. G. Tuchilus, A. F. Cristian and M. Barboiu, *J. Mater. Chem. B*, 2014, **2**, 681–690.
- 58 Y. Yang, D. Nie, Y. Liu, M. Yu and Y. Gan, *Drug Discovery Today*, 2019, **24**, 575–583.
- 59 T. Knoell, J. Safarik, T. Cormack, R. Riley, S. Lin and H. Ridgway, *J. Membr. Sci.*, 1999, **157**, 117–138.
- 60 J. Siepmann and F. Siepmann, *Int. J. Pharm.*, 2008, **364**, 328–343.
- 61 P. Misiak, K. H. Markiewicz, D. Szymczuk and A. Z. Wilczewska, *Polymers*, 2020, **12**, 2620.
- 62 T. Kaewchomphunuch, T. Charoenpichitnunt, V. Thongbaiyai, N. Ngamwongsatit and K. Kaeoket, *BMC Vet. Res.*, 2022, **18**, 1–13.
- 63 P. Singh, A. U. Mirza, A. H. Mondal, K. Mukhopadhyay and N. Nishat, *J. Appl. Polym. Sci.*, 2022, **139**, 51749.
- 64 R. Sonohara, N. Muramatsu, H. Ohshima and T. Kondo, *Biophys. Chem.*, 1995, **55**, 273–277.
- 65 P. Parvekar, J. Palaskar, S. Metgud, R. Maria and S. Dutta, *Biomater. Invest. Dent.*, 2020, **7**, 105–109.
- 66 S. Bala Subramaniam, S. Ramesh, S. Rajendran and A. Veerappan, *Bioconjugate Chem.*, 2021, **32**, 1823–1833.
- 67 R. Taheri-Ledari, M. R. Ahghari, F. Ansari, M. Forouzandeh-Malati, S. S. Mirmohammadi, S. Zarei-Shokat, S. Ramezanpour, W. Zhang, Y. Tian and A. Maleki, *Nanoscale Adv.*, 2022, **4**, 4418–4433.
- 68 A. E. Mekky and S. M. Sanad, *Bioorg. Chem.*, 2020, **102**, 104094.
- 69 M. Shahbuddin, S. S. Mahamad and R. A. Raus, *Biological and Natural Resources Engineering Journal*, 2021, **5**, 13–24.

